Experimental evidence of reaction-induced fracturing during olivine carbonation.

Experimental evidence of reaction-induced fracturing during olivine carbonation

Wenlu Zhu[1*], Florian Fusseis[2], Harrison Lisabeth[1], Tiange Xing[1], Xianghui Xiao[3], Vincent De Andrade[3], Shun-ichiro Karato[4]

[1]Department of Geology, University of Maryland, College Park, MD 20782, USA
[2]School of Geosciences, University of Edinburgh, Edinburgh, EH9 3FE, UK
[3]Advanced Photon Source, Argonne National Laboratory, Argonne, IL 60439, USA
[4]Department of Geology and Geophysics, Yale University, New Haven, CT 06511, USA

**Correspondence to*: Wenlu Zhu (wzhu@umd.edu)

Abstract. Mineral carbonation, a process that binds CO_2 in the form of carbonates by silicate weathering, is widespread on the Earth's surface. Because of the abundance of silicate rocks and the permanence of the carbonated solids, sequestering CO_2 via mineral carbonation has generated lots of interests. However, it is unclear how the fluid-rock reaction proceeds to completion in spite of an increasing solid volume. We conducted a mineral carbonation experiment in which a sintered olivine aggregate reacted with a sodium bicarbonate solution at reservoir conditions. Time-resolved synchrotron X-ray microtomographic images show cracks in polygonal patterns arising in the surface layers and propagating into the interior of the olivine aggregate. The nanotomography data reveal that the incipient cracks intersect at right angles. We infer that stretching due to non-uniform volume expansion generates polygonal cracking of the surfaces. Our data shed new lights on the processes that controls hydration and carbonation of peridotite.

Introduction

Hydration and carbonation of mantle peridotite are widespread on the surface of the Earth. Such alteration exerts controls in lithosphere strength, subduction zone geodynamics, hydrothermal circulation, water and carbon cycle. Mineral carbonation, in which CO_2 is chemically incorporated in silicate rocks to form carbonate minerals, is also recognized as a potentially safe and permanent method of CO_2 sequestration [e.g., Sefriz, 1990; Lackner, 2003] and was recently successfully tested in an industrial scale [Matter et al., 2016]. The naturally abundant mineral olivine ($(Fe, Mg)_2SiO_4$), especially its magnesium end-member forsterite (Mg_2SiO_4), has been a focus of carbon mineralization research [Goff and Lackner, 1998; Giammar

et al., 2005; Gerdemann et al., 2007; Kelemen and Matter, 2008]. Carbonation in forsterite involves the dissolution of olivine by hydrogen ions in solution,

$$Mg_2SiO_4 + 4H^+ \rightarrow 2Mg^{2+} + SiO_2(aq) + 2H_2O \quad (1)$$

followed by the precipitation of magnesite ($MgCO_3$) via reaction between magnesium and carbonate ions in solution:

$$Mg_2+ + CO_3^{2-} \rightarrow MgCO_3 \quad (2)$$

Other precipitation reactions are also possible, including formation of brucite (magnesium hydroxide) and serpentine minerals. Because the magnesium silicate is far from equilibrium with CO_2-rich fluids, aqueous mineral carbonation of olivine is one of the kinetically fastest carbonation reactions [Kelemen and Matter, 2008; Andreani et al, 2009]. The efficiency of carbon sequestration methods is mainly determined by the supply of reactive fluids and exposure of reactive solids to the CO_2-rich fluids [e.g., O'Connor et al., 2004]. The usefulness of ultramafic rocks as carbon storage thus hinges on the feasibility of creating and maintaining reactive surface area. Current implementation strategy includes grinding of solid reactants in *ex-situ* mineral carbonation reactors [e.g., Gerdemann et al., 2007; Lackner et al., 1995], hydrofracturing of the formations through *in-situ* deposition in ultramafic mines [Harrison et al., 2013; Power et al., 2013] or injection of CO_2 in basalts [Matter et al., 2016]. These processes are energy intensive and costly [Gerdemann et al., 2007; IPCC, 2005].

The hydration and carbonation of olivine results in an up to ~44% increase in solid molar volume [e.g., Kelemen and Matter, 2008]. The conventional wisdom is that unless the reaction products are deposited elsewhere, excess solids can clog fluid pathways and reduce the accessible reactive surface, causing negative feedback to halt further reaction. However, field observations show 100% serpentinization and carbonation of peridotite [e.g., Macdonald and Fyfe, 1985; Iyer et al., 2008; Beinlinch et al., 2012] even when the alteration is nearly isochemical [Kelemen and Matter, 2008]. The field data lead to a working hypothesis that excess solid reaction products could exert enough pressure (termed crystallization pressure) to break the host rocks [O'Hanley, 1992; Kelemen and Hirth, 2012]. This so-called reaction-driven cracking can create additional fluid pathways and expose new reactive surface. When reaction-driven cracking is assumed, numerical models show that olivine carbonation can proceed to completion at reasonable rates [e.g., Rudge et al., 2010]. Because natural rocks are often subjected to complex mechanical, chemical, and

thermal loads, it is unclear at what conditions these solid volume increasing reactions can proceed to completion.

Fracturing rocks via crystallization pressure is observed in salt weathering, where the salt derives from external sources [Scherer, 2004; Noiriel et al., 2010]. At reservoir conditions, however, the slow precipitation of magnesium carbonate (eqn. 2) is coupled with the rapid dissolution of olivine (eqn. 1) [Chen et al., 2006; Xu et al., 2013; Johnson et al., 2014]. The asymmetry in dissolution-precipitation kinetics renders it difficult to generate large crystallization pressure. Indeed, experimental studies of CO_2-rich brine reacting with peridotites have not produced evidence for cracking via crystallization pressure in olivine [e.g., Hovelmann et al., 2012]. Instead, laboratory studies consistently show that rates of carbonation and hydration decrease with time [O'connor et al., 2004; Andreani et al., 2009; Hovelmann et al., 2012].

Whether fracturing the solid reactants is achievable without additional energy input remains a critical question. We report on insights gained during an *in-situ* synchrotron-based X-ray microtomography (SXμT) experiment that characterized the real-time evolution of 3-dimensional (3D) pore geometry during olivine carbonation and highlight an alternative mechanism that might facilitate natural carbonation reactions.

Data Collection and Reduction

A sintered porous olivine aggregate was chosen to react with a sodium bicarbonate solution ($NaHCO_3$, 1.5 mol) at a confining pressure of 13 MPa, a pore fluid pressure of 10 MPa and a temperature of 200^{o}C (Supporting Information fig. S1). We utilized an x-ray transparent version of a Hassler core holder [Fusseis et al., 2014] to investigate the 3D microstructure evolution during olivine carbonation. The core holder was installed in a SXμT beamline at the Advanced Photon Source, where the change of rock's microstructure was recorded.

From the moment when the temperature at the sample reached 200°C, every 30 minutes 1500 projections were collected with an exposure time of 50 ms while the sample was rotated over 180° with 1.2 °s^{-1}. Between 128 and 135 hours, data were acquired in 5-minute intervals. Each dataset was acquired in 150 s. A total of 360 3D datasets amounting to 35 TB of raw data cover the entire experiment. From the radiographic projection data, 3D SXμT data with a spatial resolution of ~2 μm were reconstructed using a single-distance phase retrieval algorithm implemented in TomoPy [Paganin et al., 2002; Gürsoy et al., 2014].

After the reacted olivine sample was retrieved, Synchrotron-based X-ray nanotomography data were collected from a 65x65x63 μm^3 fragment of the post-reaction olivine aggregate, using a transmission X-ray microscope at beam line 32-ID of APS [Paganin et al., 2002]. The instrument uses an 8 keV monochromatic beam and an X-ray objective lens to magnify radiographs onto a detection system assembly comprising a scintillator (LuAG single crystal scintillator), a Zeiss 5X optical microscope objective lens and an Andor Neo sCMOS camera. The Fresnel zone plate limits the spatial resolution to 60 nm, while the voxel size is 57 nm after binning. A total of 720 projection images were acquired over a 180° rotation angle range (i.e., in 0.25° angular steps) with 2s exposure time for each image.

Because of the weak x-ray absorption contrast between magnesite and olivine at 8 keV, an iterative reconstruction method, penalized maximum-likelihood (PML) [De Carlo et al., 2014] is integrated in Tomopy [Chang et al., 2004; Gürsoy et al., 2014] to enhance the signal to noise ratio. This algorithm is proven to produce high quality reconstructions, especially for tomograms with noisy radiographs and sampling below the Nyquist criterion [De Andrade et al., 2016]. The reconstruction of a full volume with such high computational requirements method necessitates the use of a supercomputer at the Argonne Leadership Computing Facility (ALCF), where a new large-scale parallelization approach has been implemented [Biçer et al., 2015].

For geochemical analyses of the post-reaction sample, the retrieved fragments were embedded in epoxy and exposed in a polished surface. Mineral phases were identified with energy-dispersive x-ray spectroscopy in a JEOL JXA-8900 Electron probe microanalyzer operating at a 15 keV accelerating voltage and a beam current of 15 nA. Collection time for EDS data was 120 s per spot.

The reconstructed data were visualized and analyzed using the commercial software Avizo Fire. No image processing other than cropping was applied. To determine the threshold value, grey value histograms (Supporting Information, figs. S2) were computed from all analyzed time steps, smoothed, and the individual distributions superposed, following an approach described in [Fusseis et al., 2012]. The gray value distribution in each dataset is a direct function of the sample composition and changes during the reaction. Since porosity is produced, the proportion of dark voxels increases systematically at the expense of the intermediate grey voxels, causing the individual lines to intersect in a narrow region. The gray value at which the lines intersect was used for thresholding. An increase in the brightest voxels, which can also be seen in the histograms,

is a consequence of phase contrast around newly produced pores (Supporting Information, figs. S3).

Results

The SXμT time-series data provide clear evidence that the carbonation reaction progressed steadily while volume expansion and fracturing of the olivine aggregate took place as a result of olivine carbonation (Figs. 1, 2). Fine-grained reaction products precipitated in the interior of the cup wall and appear as growing clusters with smoother textures and less contrast (magenta outlines in Fig. 1). The sizes of the clusters increase with time. Nanotomography and energy-dispersive spectroscopy confirm that the precipitate clusters are formed by new carbon-rich minerals, likely magnesite (Fig. 3). Changes in the position of individual olivine grains (yellow arrows in Figs. 1, 2), which act as strain markers, are evidence for the volume expansion caused by the reaction.

Outlined by the surrounding pores, the precipitation clusters become more discernible in the tangential sections underneath the outer cup surface (Figs. 2A-E). A polygonal crack system emerges after 84 hours (Fig. 2C). In Fig. 1, it becomes apparent that the integrity of the cup wall is deteriorated by these cracks, which propagate into the cup wall from about 64 hours into the experiment. Fractures are seen to form at both the inner and outer surfaces of the cup wall (Fig. 1), and then propagate towards the interior as carbonation continues (Supporting Information, movie M1). These cracks widen to several tens of μm as reaction continues (Fig. 1) and eventually disintegrate the cup, as a post-mortem examination of the sample revealed.

Simultaneously, the total porosity evolves in the sintered cup wall (Fig. 4). The total porosity, which is normalized to the starting porosity, increases by a factor of 1.2 in both subvolumes v1 and v2 during the first 90 hours of reaction. After that, the porosity of v1 continues to increase to a factor of 1.3 until ~100 hours, when it starts a steady decline. In contrast, the porosity of v2 remains at just above 1.2, with only minor declines followed by recovery. (Fig. 4B).

We evaluated the porosity distribution within the two subvolumes by means of quantifying porosity on 2-dimensional (2D) tangential sections extracted from the segmented subvolumes along the radius of the sample (Figs. 4C&D, Supplementray Information fig. S4). At the early stages of the reaction (i.e., < 90 hours), porosity of all the tangential sections increases, likely due to dissolution of olivine grains (Figs. 4C&D). After that, porosity of the interior tangential sections decreases monotonically, consistent with the appearance of precipitants (Figs. 1, 2). In contrast,

the porosity of the 2D sections near the (inner) surface of v1 continues to increase after 90 hours (Fig. 4C). The sections near the (outer) surface of v2 exhibits similar porosity increases (Fig. 4D). The contrast between the porosity decreasing interior and the porosity increasing surfaces indicates that more reaction products are precipitated in the interior of the cup wall (cf. Fig. 1). This non-uniform precipitation corroborates with the observed total porosity changes in v1 and v2: the total porosity in v1 with more pores from the interior regions decreases, whereas the total porosity of v2 with less interior regions remains constant (Fig. 4B).

The carbonation reaction also constantly modifies the surface roughness of the olivine grains inside the cup. The rhombohedral shape of the new crystals on the surface of the olivine sand grains suggests that they are magnesite $MgCO_3$ (Fig. 5A). Both the population and size of these magnesite grains increase steadily during the entire experiment (Fig. 5B), with no indication of self-limiting behavior.

Discussion

Our experiment elucidates the real-time evolution of 3D microstructure during olivine carbonation, provides insight into the processes controlling the metamorphic reaction. Our data reveal a positive feedback between reaction progress and porosity evolution. Of particular importance is the polygonal crack pattern initiated on the surfaces of the cup wall (Figs. 1, 2). Growth of these cracks helps maintain reactive surfaces, and eventually leads to the disintegration of the sample (Supporting Information, movie M1).

Polygonal crack patterns are frequently observed in drying mud ponds [Goehring et al., 2010], cooling lava flows [Aydin and DeGraff, 1988], and ice wedge fields [Plug and Werner, 2002; Kessler and Werner, 2003] Formation of polygonal cracks requires volume mismatch between the surface and the interior of the material, which leads to a stress buildup in the surface layer [Shorling et al., 2000]. When the stress exceeds the tensile strength, cracks develop in the surface layer. Cracking at the surface results in accelerated water loss (in desiccating mud), heat loss (in cooling lava), or thermal contraction (in ice wedge) from the interior of the material. Consequently, the cracks propagate into the interior of the material. We infer these processes to have also controlled reaction advance in our experiment and may affect natural carbonation.

In our experiment, reaction advance is strongly affected by the sample geometry (Fig. 6). Dissolution of olivine in the cup wall is expected to be vigorous because smaller crystals dissolve

more rapidly [Adamson, 1990; Emmanuel and Ague, 2009]. The surge in magnesium ions in solution promotes precipitation of new crystals (Figs. 1-3). At the wall's interior, precipitation causes the infill of the pore space and solid volume expansion (Fig. 6). At the surfaces, however, the fine olivine grains in the cup wall are adjacent to the olivine sand grains, both the ones filled inside the cup as well as the ones spilled to its outside. These sand grains are ~2 orders of magnitude larger than the grains in the cup wall. Since crystallization rate negatively correlates with the curvature of the substrate [Garcia et al., 2013; Ziese et al., 2013], precipitation of new crystals preferentially takes place on the large olivine sand grains at the expense of the neighboring fine grains (Fig. 6). The lack of precipitation at the surfaces of in the cup wall is confirmed by porosity measurements (Fig. 4). The non-uniform precipitation causes the interior of the cup wall to expand faster than its surfaces, thus generating the tensile stresses necessary for cracking to occur at the surfaces (Fig. 6). The polygonal patterns (Fig. 2) suggest that the cracks are generated by the same mechanism as for the shrinkage cracks [e.g., Shorlin et al., 2000]. In our experiment, the volume mismatch between the surface and interior of the sintered olivine aggregate is instigated by rapid dissolution and non-uniform precipitation. In contrast to the crystallization pressure hypothesis, the mechanism proposed here is based on the mismatch between the volume changes in different parts of the sample and can tear the surface for tension values less than the confining pressure. Coalescence of the polygonal cracks leads to fractures disintegrating the cylindrical samples. Because of the cylindrical geometry of the samples, radial expansion is counteracted by the hoop stress it would generate. Due to this effect and the different loading systems in the axial and radial directions, the axial stress on the sample is the least compressive and the largest fractures are horizontal (Fig. 2).

In homogeneous materials, the primary shrinkage cracks intersect at right angles because the first set of cracks releases the stress normal to their surface, and consequently the second set of cracks forms perpendicular to the preexisting first set to alleviate stress in that direction [e.g., Goehring et al, 2010]. The geometric attribute can be used to verify the cracking mechanism during olivine carbonation in our experiment. Indeed, the nanotomography data of the post-reaction cup wall reveal nanometer scale cracks intersecting each other orthogonally (Supporting Information, movie M2), in good agreements with the predicted right angle of the primary cracks formed in a layer under tension [e.g., Goehring et al, 2010].

Conclusion

The time-resolved microtomography study reveals an experimentally tested mechanism for self-sustained olivine carbonation. The mechanism is the similar to that in the shrinkage cracking observed in other geological settings, though during olivine carbonation, it is the volume expansion of the interior, instead of the contraction of the surface, that causes the volume-mismatch between the surface and the interior. Compared to the crystallization pressure hypothesis, the polygonal pattern associated with tensile cracking at the surface is more consistent with fracture patterns observed in rocks that undergo natural weathering [e.g., Iyer et al., 2008]. Understanding the mechanism of reaction-induced cracking can lead to new implementation strategy of more efficient carbonation reactors. Although our experiment was conducted on porous aggregates at reservoir conditions, it is possible that cracking by the same mechanism takes place in other geological settings. In nature, carbonation of mantle peridotite can start with a pre-existing fracture network, and proceed to completion with reaction-induced cracking, as long as the non-uniform volume expansion is maintained.

References

Adamson, A.W., Physical Chemistry of Surfaces, 5th ed., Wiley, New York, 1990.

Andreani M., Luquot L., Gouze P., Godard M., Hoise E., Gibert B.: Experimental study of carbon sequestration reactions controlled by the percolation of CO2-rich brine through peridotites. Environ. Sci. Technol. 43, 1226–1231, 2009.

Aydin, A., DeGraff J.M., Evolution of polygonal fracture patterns in lava flows. Science 239, 471–476, 1988.

Beinlich A., Plümper O., Hövelmann J., Austrheim H., Jamtveit B., Massive serpentinite carbonation at Linnajavri, N–Norway. Terra Nova 24, 446-455, 2012.

Biçer, T., et al., Rapid tomographic image reconstruction via large-scale parallelization. Lecture Notes in Computer Science, 9233, 289–302, 2015.

Chang, J-H, Anderson, JMM, Votaw J.T., Regularized image reconstruction algorithms for positron emission tomography. Medical Imaging, IEEE Transactions on 23(9), 1165–1175, 2004.

239 Chen Z.Y., O'Connor W. K., Gerdemann S. J., Chemistry of aqueous mineral carbonation for
240 carbon sequestration and explanation of experimental results. Environ. Prog. 25, 161–166,
241 2006.
242 De Andrade, V., Deriy, A., Wojcik, M. J., Gürsoy, D., Shu, D., Fezzaa, K., & De Carlo, F.,
243 Nanoscale 3D imaging at the Advanced Photon Source. SPIE Newsroom.
244 doi:10.1117/2.1201604.006461, 2016.
245 De Carlo, F., et al., Scientific data exchange: a schema for hdf5-based storage of raw and analyzed
246 data. Journal of Synchrotron Radiation 21(6), 1224–1230, 2014.
247 Emmanuel, S., Ague J.J., Modeling the impact of nano-pores on mineralization in sedimentary
248 rocks. Water Resour. Res. 45, W04406, doi:10.1029/2008WR007170, 2009.
249 Fusseis F., et al., A low-cost X-ray transparent experimental cell for Synchrotron-based X-ray
250 microtomography studies at geological reservoir conditions. J. Synch. Rad. 21, 251-253,
251 2014.
252 Fusseis, F., et al., Pore formation during dehydration of a polycrystalline gypsum sample observed
253 and quantified in a time-series synchrotron X-ray micro-tomography experiment, Solid Earth,
254 3, 71-86, 2012.
255 García N.A., Register R.A., Vega D.A., Gómez L. R., Crystallization dynamics on curved surfaces.
256 Phys. Rev. E 88, 012306, 2013.
257 Gerdemann S.J., O'Connor W.K., Dahlin D.C., Penner L.R., Rush H., Ex-situ Aqueous Mineral
258 Carbonation. Environ. Sci. Technol. 41, 2587–2593, 2007.
259 Giammar D.E., Bruant R.G., Peters C.A., Forsterite dissolution and magnesite precipitation at
260 conditions relevant for deep saline aquifer storage and sequestration of carbon dioxide. Chem.
261 Geol. 217, 257-276, 2005.
262 Goehring L., Conroy R., Akhter A., Clegg W.J., Routh A.F., Evolution of mud-crack patterns
263 during repeated drying cycles. Soft Matter 6, 3562–3567, 2010.
264 Goff F., Lackner, K.S., Carbon dioxide sequestering using ultramafic rocks. Environ. Geosci. 5,
265 89-101, 1998.
266 Gürsoy D., De Carlo F., Xiao X., Jacobsen C., TomoPy: a framework for the analysis of
267 synchrotron tomographic data. J. Synchrotron Rad. 21(5), 1188-1193, doi:
268 10.1107/S1600577514013939, 2014.

269 Guyot F., Daval D., Dupraz S., Martinez I., Menez B., Sissmann O., CO2 geological storage: the
270 environmental mineralogy perspective. Compte Rendu Geosci. 343, 246–259, 2011.
271 Harrison A.L., Power I.M., Dipple G.M., Accelerated carbonation of brucite in mine tailings for
272 carbon sequestration. Environ. Sci. Technol. 47, 126-134, 2013.
273 Hovelmann J., Austrheim H., Jamtveit B., Microstructure and porosity evolution during
274 experimental carbonation of a natural peridotite. Chem. Geol. 334, 45-265, 2012.
275 IPCC, IPCC Special Report On Carbon Dioxide Capture And Storage. Cambridge University
276 Press, Cambridge UK and New York USA, 2005.
277 Iyer K., Jamtveit B., Mathiesen J., Malthe-Sorenssen A., Feder J, Reaction-assisted hierarchical
278 fracturing during serpentinization. Earth Planet Sci Lett 267, 503-516, 2008.
279 Johnson N.C., Thomas, B., Maher, K., Rosenbauer, R. J., Bird, D., & Brown, G. E., Olivine
280 dissolution and carbonation under conditions relevant for in situ carbon storage. Chem. Geol.,
281 373, 93–105, 2014.
282 Kelemen K.B., Hirth G., Reaction-driven cracking during retrograde metamorphism: Olivine
283 hydration and carbonation. Earth Planet. Sci. Lett. 345, 81-89, 2012.
284 Kelemen P., Matter, J.M., In situ carbonation of peridotite for CO2 storage. Proc. Nat. Acad. Sci.
285 105, 17295-300, 2008.
286 Kessler M.A., Werner B.T., Self-organization of sorted patterned ground. Science 299, 380-383,
287 doi:10.1126/science.1077309, 2003.
288 Lackner, K.S., Climate Change: A Guide to CO2 Sequestration. Science 300, 1677-1678, 2003.
289 Lackner K.S., Wendt C.H., Butt D.P., Joyce E.L., Sharp D.H., Carbon dioxide disposal in
290 carbonate minerals. Energy 20, 1153-1170, 1995.
291 Macdonald A.H., Fyfe W.S., Rate of serpentinization in seafloor environments. Tectonophysics
292 116, 123-135, 1985.
293 Matter, J.M. et al., Rapid carbon mineralization for permanent disposal of anthropogenic carbon
294 dioxide emissions. *Science*. 352, doi: 10.1126/science.aad8132, 2016.
295 Noiriel C., Renard F., Marie P.L., Doan M.L. Gratier J.P., Intense fracturing and fracture sealing
296 induced by mineral growth in porous rocks. Chem. Geol. 269(3-4), 197- 209, doi:
297 10.1016/j.chemgeo.2009.09.018, 2010.

O'Connor W.K., Dahlin, D.C., Rush, G.E., Gerdemann, S.J., Penner, L.R., and Nilsen, D.N., Aqueous mineral carbonation: mineral availability, pretreatment, reaction parameters, and process studies. DOE/ARC-TR-04-002, 2004.

O'Hanley D.S., Solution to the volume problem in serpentinization. Geology, 20, 705-708, 1992.

Paganin, D., Mayo, S.C., Gureyev, T.E., Miller, P.R. and Wilkins, S.W., Simultaneous phase and amplitude extraction from a single defocused image of a homogeneous object, Journal of Microscopy, 206, 33-40, 2002.

Plug L.J., Werner B.T., Nonlinear dynamics of ice-wedge networks and resulting sensitivity to severe cooling events. Nature 417, 929–933, 2002.

Power, I.M. Harrison, A., Dipple, G., Wilson, S., Kelemen, P., Hitch, M., Southam, G., Carbon mineralization: from natural analogues to engineered systems. Reviews in Mineralogy and Geochemistry 77, 305-360, 2013.

Rudge J.F., Kelemen K.B., Spiegelman M., A simple model of reaction-induced cracking applied to serpentinization and carbonation of peridotite. Earth Planet. Sci. Lett. 291, 215-221, 2010.

Seifritz, W., CO2 disposal by means of silicates. Nature 345, 486-486, 1990.

Scherer G. W., Stress from crystallization of salt. Cement and Concrete Research, 34(9), 1613–1624. doi:10.1016/j.cemconres.2003.12.034, 2004.

Shorlin K.A., de Bruyn J.R., Graham M., Morris S.W., Development and geometry of isotropic and directional shrinkage crack patterns. Phys. Rev. E. 61, 6950–6957, 2000.

Xu J., Yan C., Zhang F., Konishi H., Xu H., Teng H., Testing the cation-hydration effect on the crystallization of Ca–Mg–CO3 systems. Proc Natl Acad Sci USA 110(44), 17750-17755, 2013.

Ziese F., Maret G., Gasser U., Heterogeneous nucleation and crystal growth on curved surfaces observed by real-space imaging. J. Phys.: Condens. Matter 25: 375105, doi:10.1088/0953-8984/25/37/375105, 2013.

Acknowledgments: This material is based upon work primarily supported by the U.S. Department of Energy (DOE), Office of Science, the Office of Basic Energy Sciences (BES), Chemical Sciences, Geosciences, & Biosciences Division under Award Number DE-FG-0207ER15916; DOE, Office of Science, National Energy Technology Laboratory under Award Number DE-FE-0004375; and Royal Society Grant RG140191. This research used resources of the Argonne

Leadership Computing Facility, which is a DOE Office of Science User Facility supported under Contract DE-AC02-06CH11357. All data needed to evaluate the conclusions in the paper are present in the paper and/or the Supplementary Materials. Additional data related to this paper may be requested from the authors. We thank T. Tamarkin, G. Amulele and P. Shevchenko for sample preparation, P. Candela, and L. Montesi for discussions and I. Butler for technical assistance. We thank Dr. H. Stunitz and an anonymous reviewer for their insightful comments.

Figures

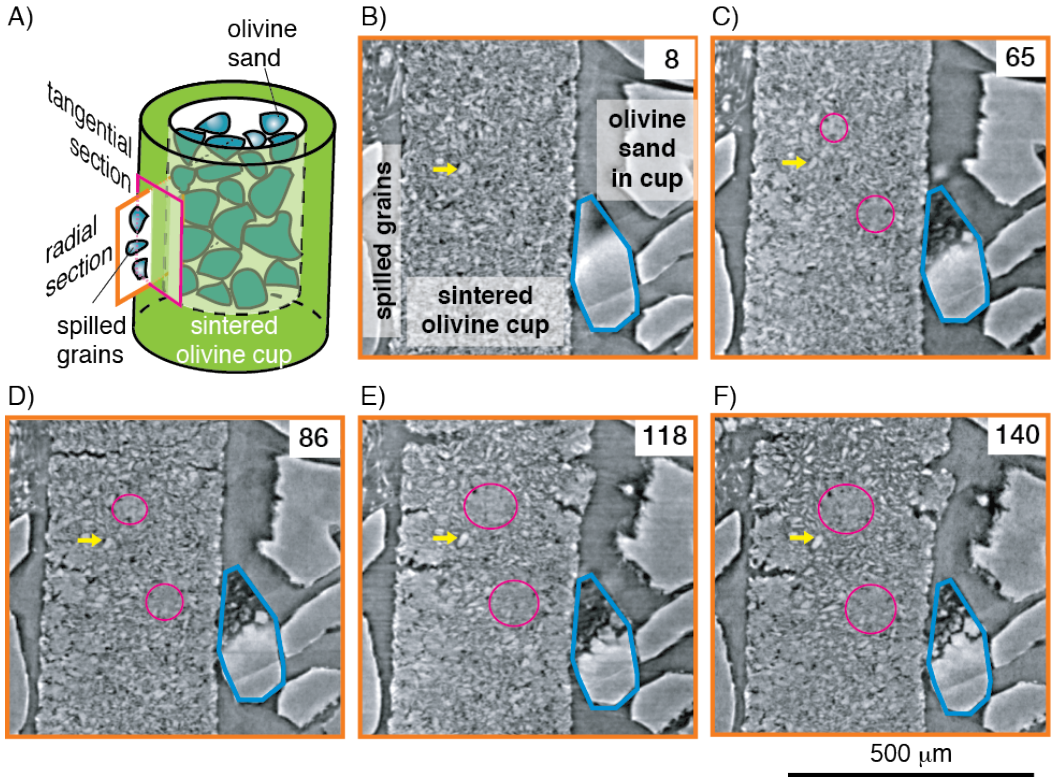

Figure 1. Temporal evolution of pore geometry in a radial section. A) A thick-walled cup (made of a sintered olivine aggregate) filled with olivine sand. Microtomographic image of a radial section (orange outline) after B) 8; C) 65; D) 86; E) 118; F) 140 hours of carbonation. Yellow arrows mark an olivine grain in the interior of the cup wall. Olivine sand grains in the cup (right side of the images) show considerable increase in surface roughness. Time series images of the surface of a representative olivine sand grain (blue outline) are presented in Figure 5. Some olivine sand grains fell between the olivine cup and the jacket during sample preparation (spilled grains on the left side of the images). Fine-grained reaction products precipitated in the interior of the cup wall appear as growing clusters with smoother textures (magenta outline). Cracks initiate at both the inner and outer surfaces of the cup wall after 64 hours of reaction. Cracks widen as reaction continues.

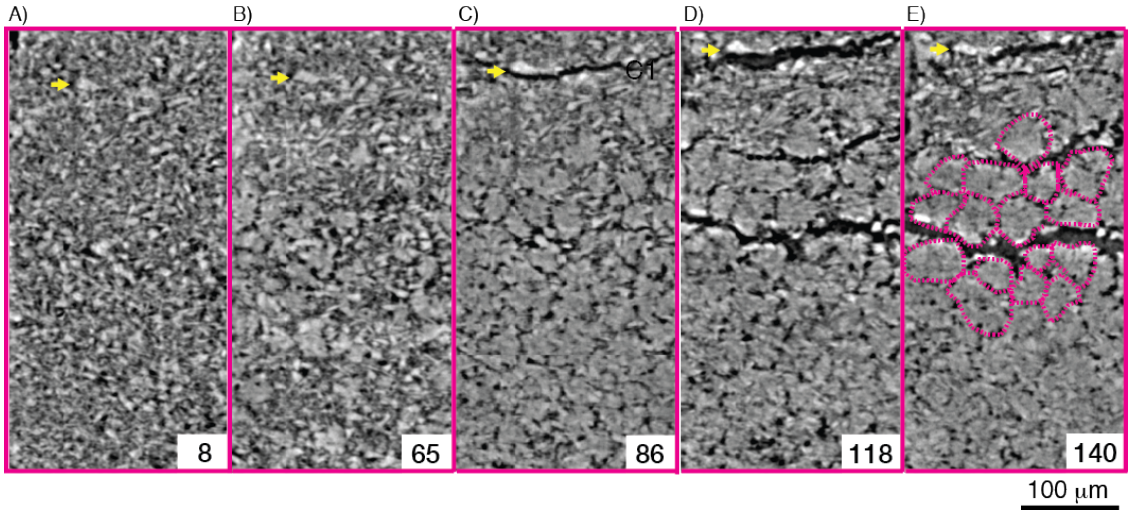

Figure 2. Temporal evolution of pore geometry in a tangential section. Microtomographic image of a tangential section of the olivine cup (magenta outline in Fig. 1A) undergoing A) 8; B) 65; C) 86; D) 118; E) 140 hours of carbonation. Yellow arrows mark an olivine grain in the interior of the cup wall. Its position change with respect to the top of the image window (fixed) serves as a strain marker for the volume expansion resulting from reactions. In the tangential section, polygonal cracks develop along the edge of the reactant clusters (magenta outline). Coalescence of the polygonal cracks leads to fractures across the aggregate.

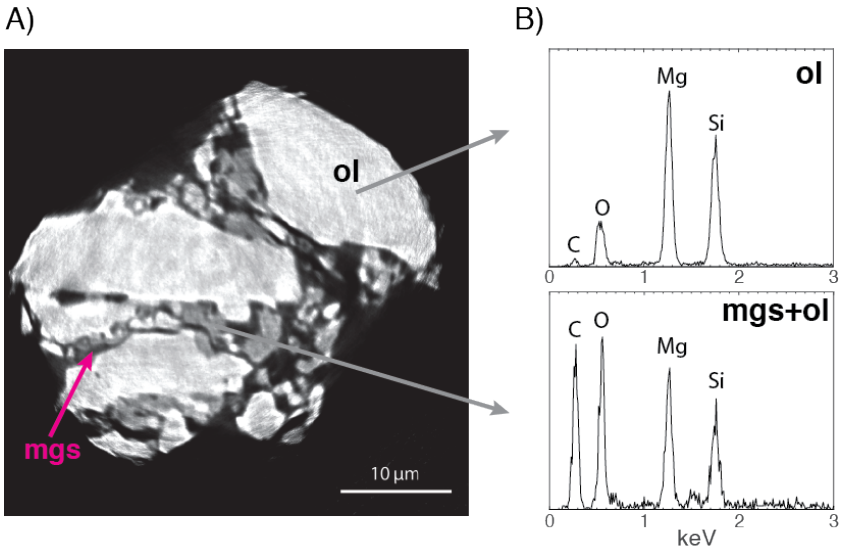

Figure 3. Segment of the post-reaction cup wall. A) A 2D nanotomographic image shows that new phases (mgs, dark grey) precipitate in the pore space between olivine grains (ol, light grey) of the olivine aggregate; B) EDS data of the post-reaction cup wall. The weak carbon signal in the spectrum of olivine grains results from carbon coating. In contrast, the spectrum of the regions filled with precipitants (mgs+ol) shows significant carbon content, which suggests epitaxial magnesite (mgs) growth on the olivine grains (ol).

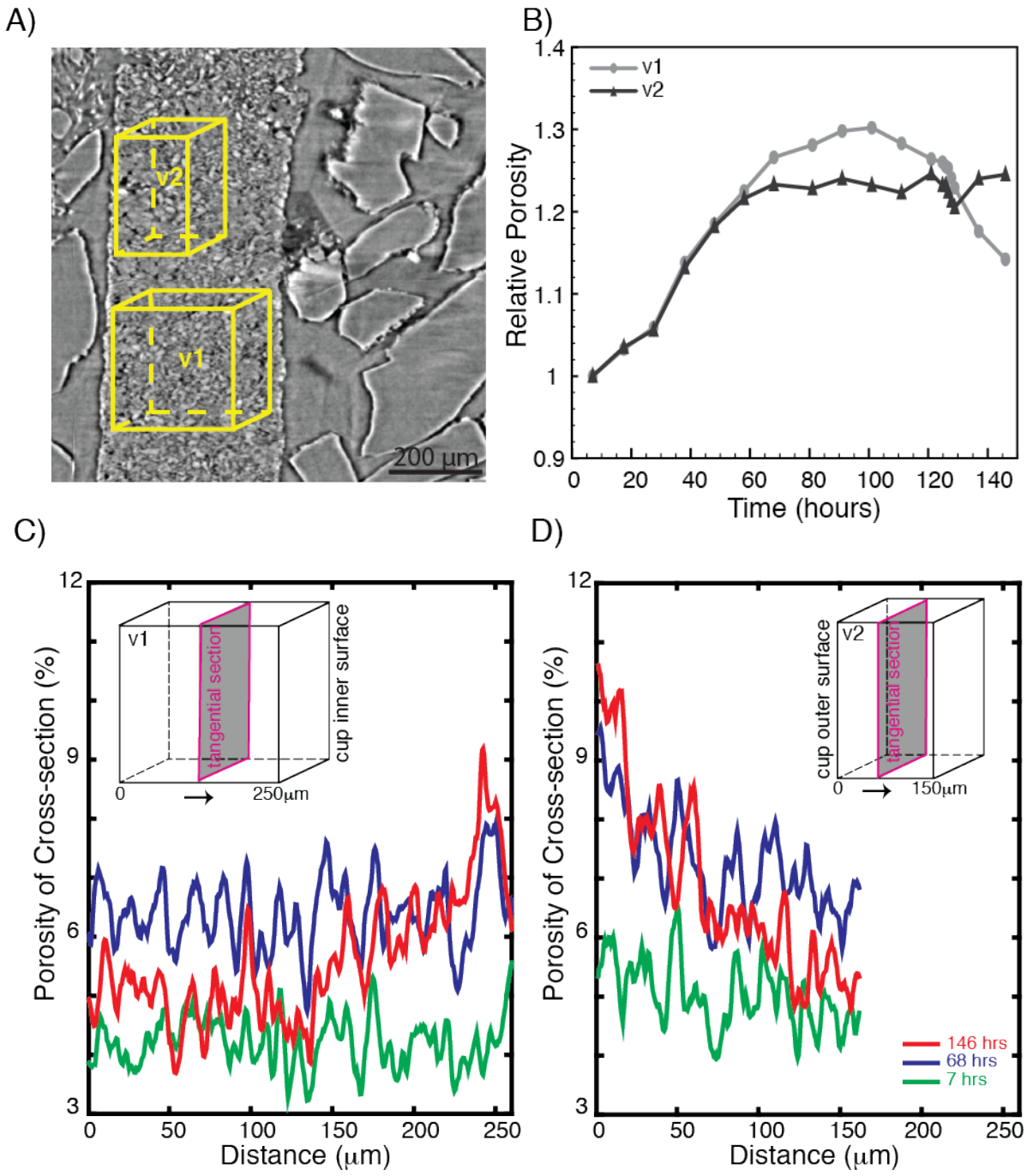

Figure 4. Porosity evolution of subvolumes. A) Subvolumes v1 and v2; B) Relative porosity change of v1 (light grey) and v2 (dark grey) during 146 hours of olivine carbonation. C) Porosity evolution of 2D tangential sections (magenta slice) taken from C) subvolume v1; D) subvolume v2 after 7 (green), 68 (blue), 146 (red) hours of reactions. Note that the leftmost edge of subvolume 2 is at the outer surface of the olivine cup wall, the rightmost edge of subvolume 1 is at the inner surface of the cup wall. Porosity at the interior first increases and then decreases during carbonation, whereas porosity near both the outer and inner surfaces increases.

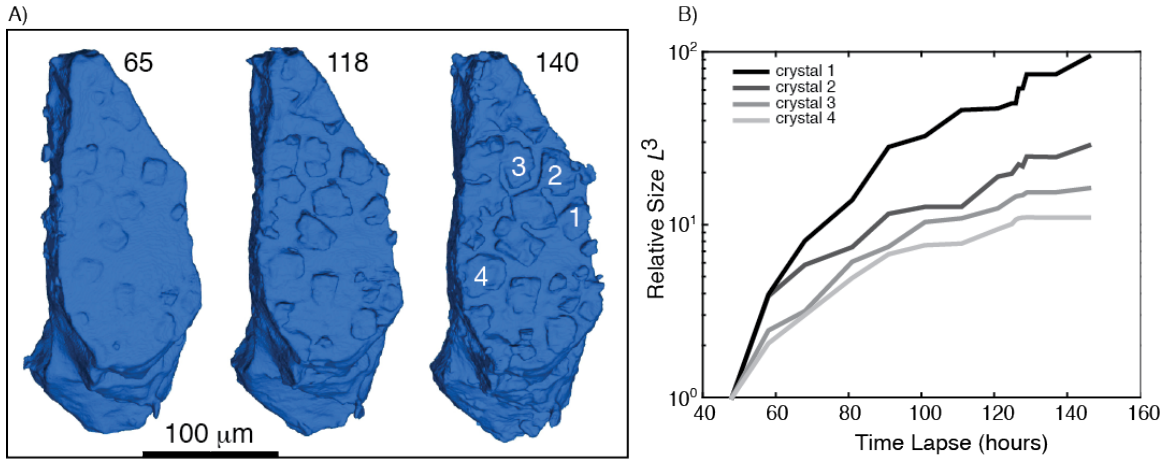

Figure 5. Nucleation and growth of new crystals. A) Surface of a representative olivine sand grain (blue outline in Fig. 1) in the olivine cup; B) Cubic circumferential length L (normalized to that at 48 hours of carbonation when most of the new crystals first appeared) of several new crystals as a function of time.

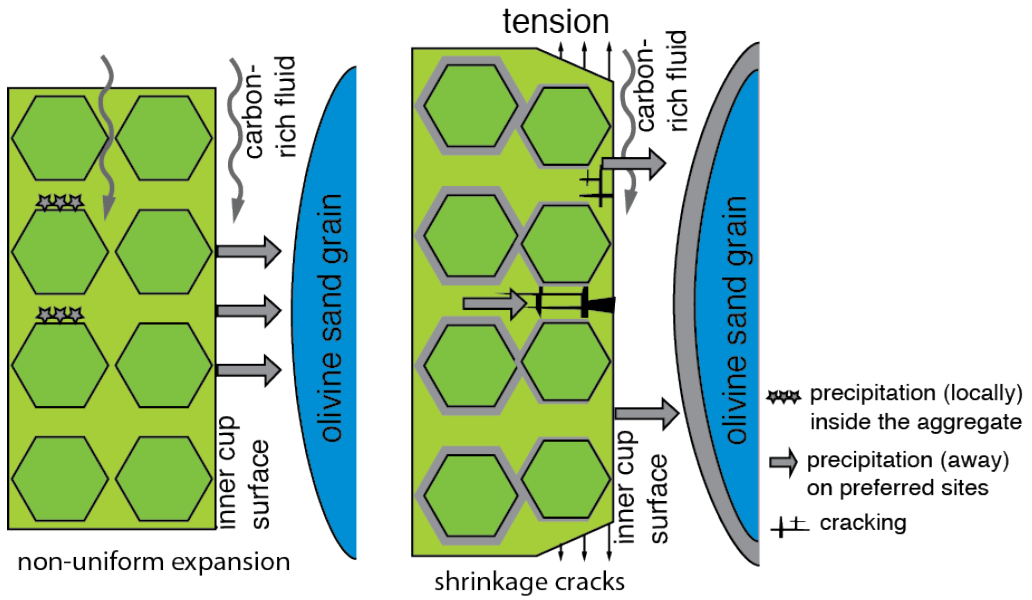

Figure 6. Schematic diagram for shrinkage cracking during mineral carbonation. At the surface of the fine-grained olivine aggregate (green), reactants (grey) preferentially precipitate on the large olivine sand grains (blue). Beneath the surface of the cup wall, reactants precipitate locally (grey stars), leading to non-uniform volume expansion. As the reaction continues, cracks form in response to increasing strain.